Chapter 8
Grain Boundary Phase Transformations in Nanostructured Conducting Oxides

B.B. Straumal, A.A. Myatiev, P.B. Straumal, and A.A. Mazilkin

Abstract Nanostructured conducting oxides are very promising for various applications like varistors (doped zinc oxide), electrolytes for the solid oxide fuel cells (SOFC) (ceria, zirconia, yttria), semipermeable membranes, and sensors (perovskite-type oxides). Grain boundary (GB) phases crucially determine the properties of nanograined oxides. GB phase transformations (wetting, prewetting, pseudopartial wetting) proceed in the conducting oxides. Novel GB lines appear in the conventional bulk phase diagrams. They can be used for the tailoring of properties of nanograined conducting oxides, particularly by using the novel synthesis method of liquid ceramics.

8.1 Introduction

Conducting oxides are currently broadly used for various applications, e.g., zinc oxide for manufacturing of varistors [1, 2], ruthenates as thick-film resistors [3], oxides of fluorite structure (ceria, zirconia, yttria) as electrolytes for the solid oxide fuel cells (SOFC) and oxygen sensors [4], perovskite-type oxides ($BaTiO_3$, $SrTiO_3$, $LaAlO_3$, $LaCrO_3$, etc.) as electrolytes and electrodes for SOFC, semipermeable membranes, and sensors [5]. Other applications of semiconducting oxides are various electronic devices such as self-controlled heaters, color TV degaussers, fuel evaporators, and air-conditioning equipment [6].

The electrical properties of these oxides, especially of nanostructured ones, are crucially determined by the structural and chemical characteristics of the grain boundaries (GBs). It can be due to the formation of: (a) conventional GB segregation layer with a content of a second (third, fourth etc.) component less than one monolayer (ML); (b) thin (few nm) continuos layer of a GB phase, which can be described also as multilayer segregation, and (c) thick (several micrometers and more) layer of a solid, liquid, or amorphous wetting phase. Such GB layers may be thermodynamically stable, metastable, or unstable. Therefore, it is of crucial importance, to have at disposal the phase diagrams including the lines of bulk and GB phase transformations. Such diagrams allow tailoring the synthesis of nanostructured oxides, controlling their microstructure and producing the devices with stable properties and long life-time.

H. Hahn et al. (eds.), *Nanoscale Phenomena: Fundamentals and Applications*,
NanoScience and Technology, DOI 10.1007/978-3-642-00708-8_8,

8.2 Grain Boundary Phase Transformations and Phase Diagrams

Let us consider the schematic two-component eutectic phase diagram describing the conditions for the thermodynamic equilibrium for all three cases listed earlier. Thermodynamically stable GB layers form as a result of the so-called GB phase transitions, GB wetting being an important example of such processes [7, 8]. GB wetting phase transitions have recently been included in the traditional phase diagrams of several systems [9, 10]. The occurrence of wetting depends on the GB energy, σ_{GB}. Consider the contact angle Θ between a bicrystal and a liquid phase. When σ_{GB} is lower than $2\sigma_{SL}$, where σ_{SL} is the energy of the solid–liquid interphase boundary, the GB is nonwetted and $\Theta > 0°$ (point 1 in Fig. 8.1). However, if $\sigma_{GB} \geq 2\sigma_{SL}$, the GB is wetted and the contact angle $\Theta = 0°$ (point 2). The temperature dependency of $2\sigma_{SL}$ is stronger than that of σ_{GB}. If the curves describing the temperature dependencies of σ_{GB} and $2\sigma_{SL}$ intersect, the GB wetting phase transition will occur upon heating at the temperature, T_w, of their intersection. At $T \geq T_w$, the contact angle is $\Theta = 0°$. By crossing the bulk solidus between points 2 and 3, the liquid phase becomes metastable. Its appearance in the system costs the energy loss Δg. The energy gain (σ_{GB}–$2\sigma_{SL}$) above T_w can stabilize the GB liquid-like layer of a thickness l. By moving from point 3 to point 4, the energy loss Δg increases and the GB liquid-like layer disappears at GB solidus line. Therefore, the stable layer of liquid-like phase (which is unstable in the bulk) can exist in the GB between bulk and GB solidus lines (point 3). The same is true also if the second phase is solid. In point 2′ GB in the α-phase has to be substituted by the layer of

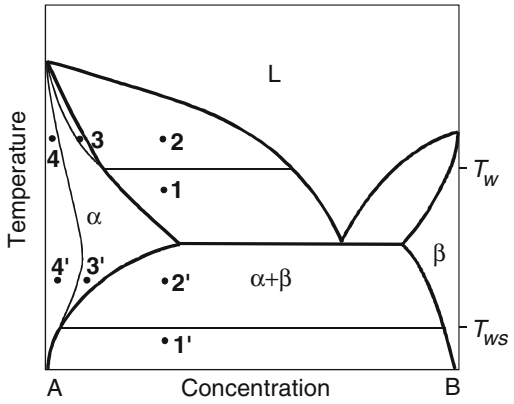

Fig. 8.1 Schematic phase diagram with lines of GB phase transitions. T_w – temperature of the GB wetting phase transition (proceeds between points 1 and 2). T_{ws} – temperature of the GB solid phase wetting transition (proceeds between points 1′ and 2′). Between points 3 and 4 the GB premelting phase transition occurs. Between points 3′ and 4′ the GB premelting phase transition occurs. In points 3 and 3′ GB is covered by the equilibrium layer of a liquid-like or β-like phase which is unstable in the bulk

β-phase and two α/β interphase boundaries (IBs). In point 3′ GB is covered by the equilibrium layer of a β-like phase that is unstable in the bulk. In points 4 and 4′ GB is "pure" and contains only the usual segregation layer of component B. Therefore:

(a) Conventional GB segregation layer with a content of a second (third, fourth etc.) component less than one ML exists in areas marked by points 4 and 4′;
(b) Thin (few nanometres) continuous layer of a GB phase exists in areas marked by points 3 and 3′ and
(c) Thick (several micrometres and more) continuous GB wetting layer of a liquid or solid phase exists in areas marked by points 2 and 2′.

This simple scheme permits to understand the phenomena in numerous conducting oxides. Very often, they are produced with the aid of the liquid phase sintering, where all GBs are wetted by liquid phase (i.e., in the area 2 of the scheme in Fig. 8.1). By the following cooling, the GB melt layer solidifies and can transform either into an array of droplets, or into amorphous GB layer, or into crystal wetting phase, or into conventional GB segregation layer of less than one ML. In detail, the GB phases and GB structure in conducting oxides determining their life-time and properties strongly depend on the composition and the processing route.

8.3 Grain Boundary Phases in Zinc Oxide

Zn oxide is mainly used for manufacturing varistors. Varistors exhibit highly nonlinear current–voltage characteristics with a high resistivity below a threshold electric field, becoming conductive when this field is exceeded, enabling them to be used in current over-surge protection circuits [11]. The model usually proposed to account for the electrical properties of ZnO-based varistors is constituted on the basis of a bricklayer. ZnO-based varistors are approximated as a stacking of good conducting grains separated by GBs, which support back-to-back double Schottky barriers [12–14]. Polycrystalline zinc oxide contains small amounts of dopants, mainly bismuth oxide. After liquid-phase sintering, such material consists of ZnO grains separated by the Bi_2O_3-rich GB layers. Interfaces between the ZnO grains control the nonlinear current–voltage characteristics. Although the Schottky barriers at ZnO/ZnO boundaries mainly control the voltage-dependent resistivity of a varistor, the Bi-rich GB phase also inputs into the overall resistivity.

The intergranular phase originates from the liquid-phase sintering. The sintering conditions alter the performances of ZnO varistors [13]. An increase in the sintering temperature results usually in a lowering in the nonlinearity of the current–voltage curve. Bhushan et al. pointed out that an increase in the sintering temperature would lower the Schottky barrier height [15] and Wong mentioned that the volatilization of Bi_2O_3 during the sintering would bring a loss in the nonohmic property of the varistors [16]. The big amount of structural investigations permitted us to construct the GB lines in the ZnO–Bi_2O_3 bulk phase diagram (Fig. 8.2) [1, 17–25]. The first variant of the ZnO–Bi_2O_3 phase diagram has been experimentally constructed by

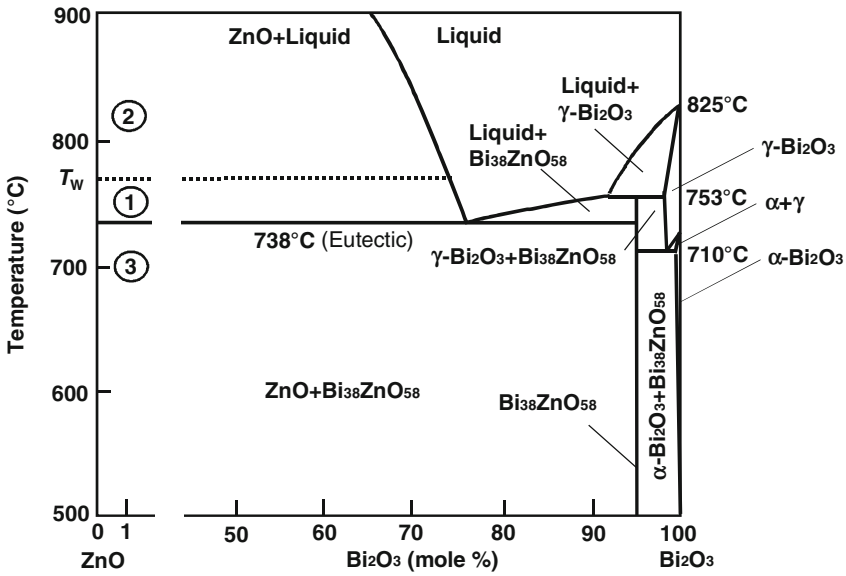

Fig. 8.2 ZnO–Bi_2O_3 phase diagram (*solid lines*, [27]). Tie-line of GB wetting phase transition slightly at T_w above eutectic temperature T_e is added to the bulk diagram (*dotted line*). In the area (1) between T_e and T_w melt partially wets the ZnO GBs [1]. In the area (2) above T_w melt fully wets the ZnO GBs [5]. In the area (3) below T_e ZnO GB triple junctions contain crystalline Bi_2O_3 and ZnO GBs contain amorphous Bi-rich phase with about 25–30 mol.% Bi (see scheme in Fig. 8.3b) [1, 17]

Safronov et al. [26]. However, recently Guha et al. [27] found new γ-Bi_2O_3-phase and refined the ZnO–Bi_2O_3 phase diagram (Fig. 8.2).

The liquid phase sintering of the ZnO + Bi_2O_3 mixture proceeds in the ZnO + liquid region of the ZnO–Bi_2O_3 phase diagram, i.e., above eutectic temperature of $T_e = 738°C$ (usually at 850°C) [1]. During the liquid phase sintering, all ZnO/ZnO GBs are completely wetted by the thick layer of the melt. The thickness of the melt layer is governed only by the grain size and amount of the liquid phase (i.e., on the Bi_2O_3 content). At 850°C, the liquid phase completely wets not only all ZnO/ZnO GBs, but also the free surface of the ZnO particles [17]. There is some indications that in the ZnO + liquid region close to T_e, the complete GB wetting transforms into partial GB wetting (with contact angles above zero) [1]. In other words, in the ZnO–Bi_2O_3 phase diagram, the GB wetting tie-line exists slightly above T_e (Fig. 8.2).

The quenching from 850°C leaves a thick intergranular phase at the ZnO/ZnO GBs. However, the slow cooling below T_e leads to the dewetting of ZnO/ZnO GBs by crystallization of Bi_2O_3 [18–21]. Since the optimization of the varistor properties needs the slow cooling or a low-temperature post annealing, much work was devoted to the structure of GBs in varistors [20–22]. At the beginning of these investigations, it was believed that all GBs contain thin Bi-rich intergranular phase.

Then Clarke reported that most ZnO GBs in a commercial varistor were free from the second-phase films, and the atomically abrupt GBs were observed using the lattice fringe imaging [28]. However, later Olsson et al. found the continuous Bi-rich films in the majority of ZnO/ZnO GBs, and only a few GBs were atomically ordered up to the GB plane [23, 24]. It was also found that the treatment at high hydrostatic pressure of 1 GPa leads to the desegregation of ZnO/ZnO GBs [25]. During desegregation, the Bi-rich GB phase disappears due to the Bi GB diffusion toward the secondary phase in the GB triple junctions.

Wang and Chiang studied the ZnO with 0.23 mol% at Bi_2O_3 700°C [1]. The samples were brought into equilibrium at this temperature from three different starting points: (a) after liquid phase sintering at 850°C followed by 24 h annealing at 700°C and slow cooling down to the room temperature; (b) by sintering directly at 700°C (i.e., below T_e, without presence of any liquid phase) for 2 h by 1 GPa followed by the annealing at 700°C at the room pressure; and (c) equilibrium segregation at 700°C was reached from the high-pressure desegregated state. Wang and Chiang discovered that in all the three cases the equilibrium GB state at 700°C is the amorphous intergranular film of 1.0–1.5 nm in thickness. In other words, a thin intergranular film has a lower free energy in comparison with pure crystal–crystal GB. The thermodynamic conditions for the existence of such films were studied by Clarke [29]. After desegregation at high temperature (Fig. 8.3a), GBs are free from any Bi-rich layers (thin or thick). Crystalline Bi_2O_3 particles are present in the GB triple junctions. However, after additional annealing at the same temperature of 700°C but at atmospheric pressure, Bi diffuses back from the triple junctions into the GBs forming the amorphous GBs films of 1.0–1.5 nm in thickness (Fig. 8.3b). In other words, the amorphous films build not from the undercooled liquid, but in the solid phase, as a result of Bi GB diffusion. Moreover, the thin amorphous film covers not only the ZnO/ZnO GBs, but also the intrephase boundary between ZnO grains and Bi_2O_3 particle in the ZnO GB triple junction (Fig. 8.3b).

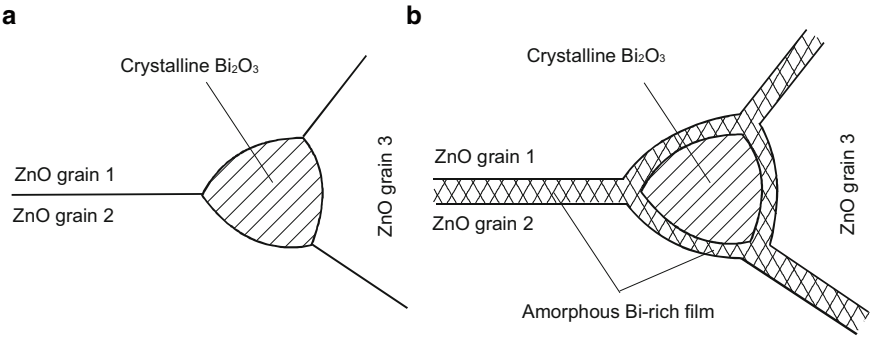

Fig. 8.3 Scheme of GBs and GB triple junction in the ZnO–Bi_2O_3 at 700°C [1]. (**a**) Structure after pressure desegregation at 1 GPa. GB triple junction contains lenticular crystalline Bi_2O_3 phase. GBs contain no films. (**b**) Structure after additional anneal at atmospheric pressure. GBs contain amorphous Bi_2O_3-rich film of 1–2 nm thickness with about 25–30 mol.% Bi. Similar film separates ZnO grains and the lenticular crystalline Bi_2O_3 phase in the GB ZnO triple junction

This behavior can be explained by the so-called pseudopartial wetting [17, 30]. At certain thermodynamic conditions, liquid droplets have a nonzero contact angle with a solid substrate (or a GB), but the rest of a substrate surface (or a GB) is not dry, but covered by a thin film of few nm thickness. For example, the liquid Bi-rich nanodroplets (5–15 nm) with contact angle of about 40° were observed on the top of the amorphous film of 1.95 nm thickness on the ZnO surface facets [17].

8.4 Conducting Oxides of Fluorite Structure

Conducting oxides of fluorite structure have received much attention in recent years due to their ionic conductivity with the applications as electrolytes for the SOFC and oxygen sensors. Yttria-stabilized zirconia (YSZ) is by far the most widely used solid electrolyte for technological applications. The main factors driving the interest for this solid electrolyte are its high chemical stability in oxidizing or reducing environments and its compatibility with a variety of adjoining electrode materials. It is presently employed at temperatures above 600°C. Other oxides like calcia or scandia can also be used for the stabilization of zirconia. Although stabilized zirconia exhibits good conductivity at high temperatures, the need for a better oxygen-conducting material in SOFCs has shifted interest to doped ceria [31], which exhibits good conductivity at lower temperatures. Usual doping ions for CeO_2 are Gd^{3+}, Sm^{3+}, and Y^{3+}. Substitution of the Ce^{4+} cations in the lattice results in the formation of vacancies and enhances the ionic conductivity.

8.4.1 GB Wetting Phases

It has been shown that the maximum of the ionic conductivity of YSZ occurs around 9.5 mol% Y_2O_3 [32,33]. Measurements of conductivity and oxygen diffusivity confirmed that YSZ are the ionic conductors at the temperatures as low as 200°C [34]. Critical to the low-temperature applications are the internal interface properties of YSZ. In YSZ, a glassy phase was commonly observed in GBs and GB triple junctions. In [38] two YSZs (called Z_C and Z_F) were sintered from powders prepared through two different processing routes. In samples Z_C the glassy phase wetted GBs and GB triple junctions. Glassy phase in triple junctions has a shape of stars with zero contact angles at GBs. These "stars" continue toward GBs as GB wetting layers. In samples Z_F, the amorphous precipitates of glassy phase in triple junctions are lenticular, and spherical glass pockets are widely dispersed in the bulk of grains, but there is no evidence of glassy films at GBs. As a result, the GB conductivity of the Z_F polycrystal, which shows glass-free GBs, is about three orders of magnitude higher than that of the Z_C material (Fig. 8.4). These results are consistent with the mechanism of oxygen-ion transport across GBs suggested by Badwal [35]. Conductivity occurs without any constriction of current pathways in the Z_F

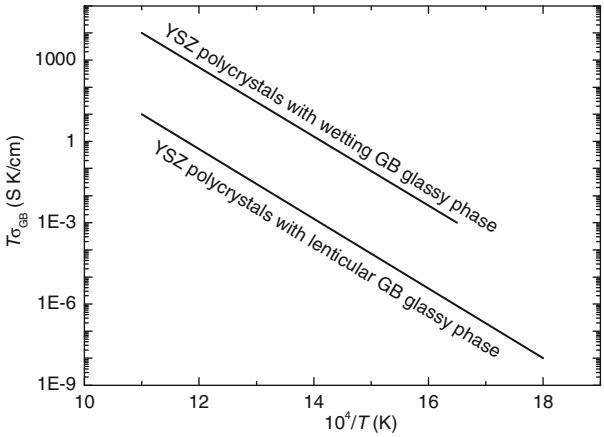

Fig. 8.4 Temperature dependence of specific GB conductivity of YSZ polycrystals with and without GB glassy phase according to the data of [34]

ceramics, while it is restricted to the unwetted GBs in the Z_C ceramics. Therefore, if a GB wetting phase is detrimental, one can change a composition in such a way that the GB wetting conditions are not fulfilled any more. In this case the GB network of detrimental phase is broken and the properties of a material improve. Thus, by changing GB wetting conditions by microalloing, one can improve the properties of a conducting oxide.

8.4.2 Monolayer GB Segregation

Even in the absence of the GB layers of wetting phases, the properties of conducting oxides can be controlled by the conventional (less that one ML) GB segregation. In the zirconia obtained by the conventional sintering methods, a minor amount of silicon, originated from contaminated starting materials, detrimentally influences the conductivity of fuel cells oxides [36]. This effect originates from silicon coverage of GBs in stabilized zirconia with the formation of a continuous GB network in the polycrystal. Silicon-containing phase forms lenticular GB particles and they do not wet the GBs. However, if the Si concentration in GBs reaches about 0.5 ML, the GB conductivity drastically decreases, and does not change much with a further increase of GB Si content [36]. However, if the grain size in stabilized zirconia decreases from micrometer into the nanometer range, the amount of silicon will not be enough to contaminate all GBs. As a result, the specific GB conductivities in nanocrystalline calcia-stabilized zirconia increase about five times [36]. The specific GB conductivities of the nanocrystalline YSZ samples (grain size 40 nm) are 1–2 orders of magnitude higher than those of the microcrystalline samples (grain size 400–1,000 nm) (Fig. 8.5) [37]. Therefore, the detrimental effect of Si-contamination

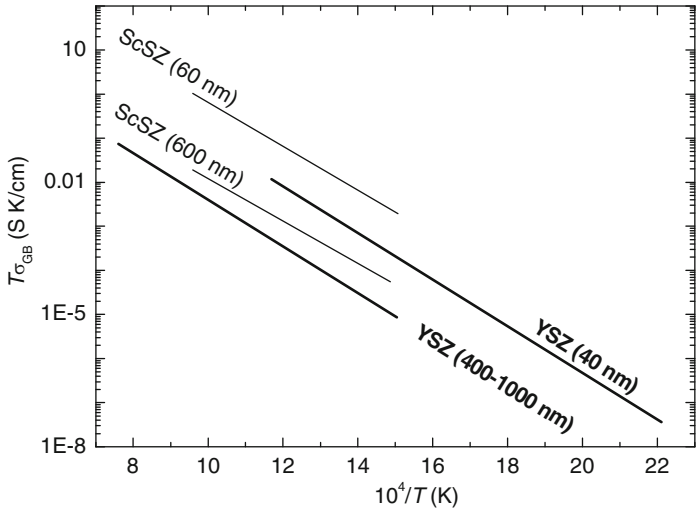

Fig. 8.5 Temperature dependence of specific GB conductivity in nano- and microcrystalline zirconia stabilized by yttria and scandia. Specific GB conductivity increases by decreasing of grain size. Thick lines represent the data of [37] for yttria-stabilized zirconia. Thin lines represent the data of [38] for scandia-stabilized zirconia

vanishes and overall properties of nanostructured zirconia improve. Similar effect of grain size was observed in the scandia-stabilized zirconia [38]. The specific GB conductivities measured using the impedance spectroscopy increase almost two orders of magnitude when grain size decreases from 6,000 to 60 nm (Fig. 8.5). It is an important example, how the GB engineering (tailoring the polycrystal properties by controlling the GB structure and composition) can improve the properties of nanostructured oxides for fuel cells. Thus, by decreasing the grain size, one can dilute the detrimental GB segregation down to the harmless value and improve the properties of a conducting oxide.

8.4.3 Scavengers for GB Impurities

Another way to compensate for the detrimental Si influence and to improve the GB conductivity in zirconia and ceria is to use the so-called scavengers. It has been shown already in 1982 that small additions of Al_2O_3 drastically improve the ionic conductivity of YSZ [39]. Later, Al_2O_3 was identified as the most effective dopant in increasing the GB conductivity of zirconia-based electrolytes [40–43]. Butler and Drennan suggested that alumina acts as a "scavenger" for SiO_2, since the affinity of SiO_2 to Al_2O_3 is greater than to the ZrO_2 [39]. As a result, the particles of Al_2O_3 present in the ceramic "sweep out" silicon from zirconia GBs. It results in

the purification effect similar to that of the decrease of grain size. The best scavenger for ceria-based electrolyte is the iron oxide [44].

8.4.4 Heavy Doping

Heavy doping is another way to change the GB composition, and therefore, to improve the conductivity of an oxide. Cerium oxide is a mixed ionic/electronic conductor and exhibits high ionic conductivity when doped with lower valent cations (acceptors). As the oxygen vacancy mobility is even higher than in cubic zirconia – the other prominent fluorite-structured oxygen ion conductor – there has been considerable interest in the potential of ceria-based solid electrolytes for applications in SOFC or oxygen membranes. In [45] the microcrystalline ceria was doped with Y, La, and Gd in the broad concentration range between 0.1 and 27 at.%. The GB effect, which is indicated by the gap between the bulk and the total conductivity, was found to decrease rapidly as the acceptor concentration increases. The GB conductivity drastically increases at the acceptor concentration between 2 and 10 at.% (Fig. 8.6). Simple estimation reveals that the GB conductivity reaches the bulk value when all GBs become covered with a ML of an acceptor impurity (for the ceria grain size of about 1μm).

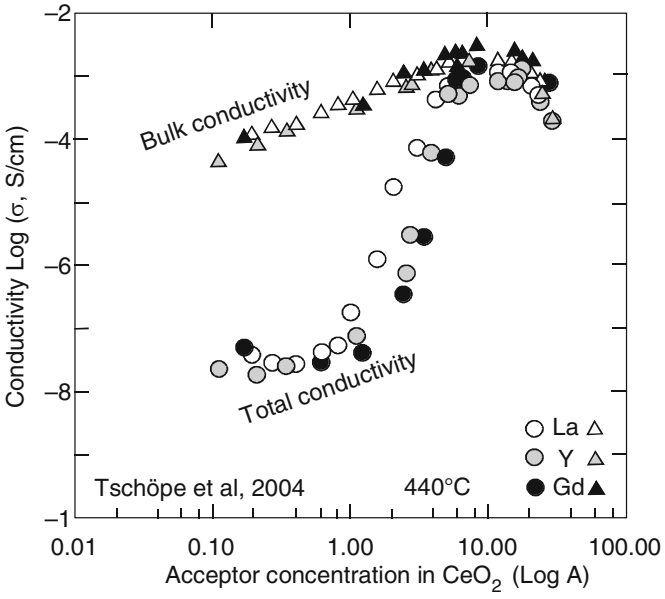

Fig. 8.6 Bulk (*triangles*) and total (*circles*) electrical conductivities at $T = 440°C$ of La-, Y- and Gd-doped microcrystalline cerium oxide as function of dopant concentration according to the data of [45]

8.5 GB Phenomena in Perovskites

Perovskite-type oxides ($BaTiO_3$, $SrTiO_3$, $LaAlO_3$, $LaCrO_3$, etc.) have recently attracted considerable attention for their applications in high-temperature electrochemical devices, such as electrolytes and electrodes of SOFC, oxygen permeating membranes, sensors etc. For the ionic conduction, some perovskites exhibit surprisingly high ionic conductivities, higher than those of well-known zirconia-based materials. The impedance spectroscopy permits to separate bulk and GB inputs in overall conductivity. In many cases, the overall conductivity of perovskites is determined by the GB resistance, like that of Sr and Mg doped $LaAlO_3$ below 550°C [6]. However, the GB input into overall conductivity gradually decreases by increasing temperature. GBs in perovskites mainly contain the conventional GB segregation layer. Only in few cases (like in $BaTiO_3$ sintered from powder particles with Mn coating), the GB amorphous region with a width of about 1 nm was observed [5]. The boundary width in such polycrystals is about five times larger than that in the $BaTiO_3$ sintered from powder particles without Mn coating. The electrostatic potential barrier height of the $BaTiO_3$ ceramics increased from 0.18 to 0.24 eV, due to the increase in the width of the excess negative charge layer from 70 to 120 nm, with an increase in the amount of the powder coating material from 0 to 1.0 at.%. A systematic variation of the GB features with the amount of coating material indicates the possibility of using this synthesis method to get fine control over the chemistry and electrical properties of the semiconducting $BaTiO_3$ ceramic.

8.6 Influence of Synthesis Route on the Properties of Nanostructured Materials

The unique properties of nanostructured materials (including those of nanograined conducting oxides) are of great importance for various advanced applications. However, there are some indications that physical properties of the same material with the same grain size in a nanometer range depends drastically on the preparation technique.

It is well known that during the manufacture of nanostructured materials, the amorphisation may happen, the supersaturated solid solutions may appear, the metastable phases may form [46]. However, there are indications that physical properties of the same material with the same grain size in a nanometer range depend on the preparation technique. The most reliable data on the formation of metastable phases came from the ball-milling experiments. Particularly, the ball milling of steels reliably and reproducibly leads to the dissolution of cementite or the formation of amorphous solid solution in steels [47–50]. Implantation of carbon ions into iron also produces the strongly nonequlibrium structure in surface layers of samples [51]. In other words, ball milling also called mechanical alloying can be compared with a kind of mechanic implantation of one material into another. The high-pressure torsion (HPT, also called compression shear) or deep drawing is

principally different from the ball milling. The investigations on HPT of Al-based alloys [52, 53] demonstrated that HPT or deep drawing lead simultaneously (a) to the formation of highly nonequilibrium nanometer grain structure and (b) to the disapperance of nonequlibrium phases and the formation of phases that are in equlibrium at the HPT temperature and pressure. The carefull experiments and analysis of previous publications on HPT demonstrate that HPT leads to the grain refinement, but cannot lead to the disappearance of equlibrium phases or the formation of nonequlibrium phases. It is the most important difference between HPT and ball milling as two technologies for the manufacture of nanostructured materials. Therefore, the application of various novel techniques for the manufacture of nanograined conducting oxides is very promising, especially when they permit to synthesize the novel stable GB phases.

8.7 Synthesis of Nanostructured Oxides by a "Liquid Ceramics" Method

Nowadays the majority of conducting oxides are produced by the sintering of oxide powders. The addition of oxides with low melting points as sintering adds is used for liquid-phase sintering. Sintering has several disadvatages, particularly it includes the high-temperature synthesis steps and leads to the easy contamination of sintered oxides (especially by silicon). New synthesis technologies would permit to broaden the spectrum of oxides and to produce compounds with properties very promising for the SOFCs and electronic components.

Recently, the novel technology has been developed for the deposition of multicomponent oxide films from organic precursors (so-called liquid ceramics) [54]. The films can be deposited on various substrates. The deposited films of ZnO, Y_2O_3, and Ce–Gd–Ni complex oxide are dense, nonporous, nanostructured, uniform, nontextured (Figs. 8.7 and 8.8). Grain size in these films can be varied from

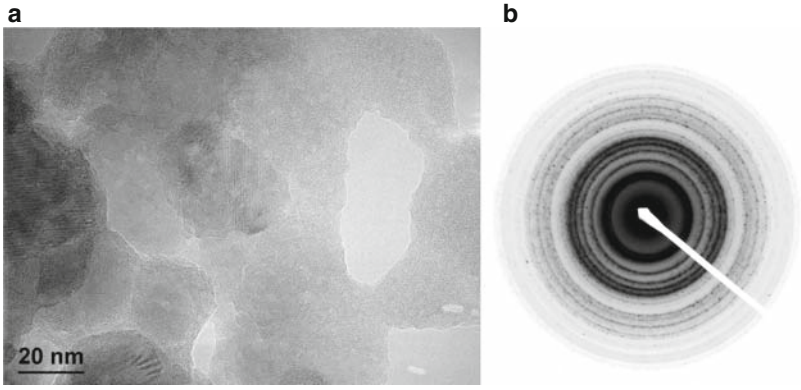

Fig. 8.7 (**a**) Bright field high-resolution electron micrograph of the nanograined ZnO thin film deposited by the liquid ceramics technology and (**b**) Electron diffraction pattern. No texture is visible

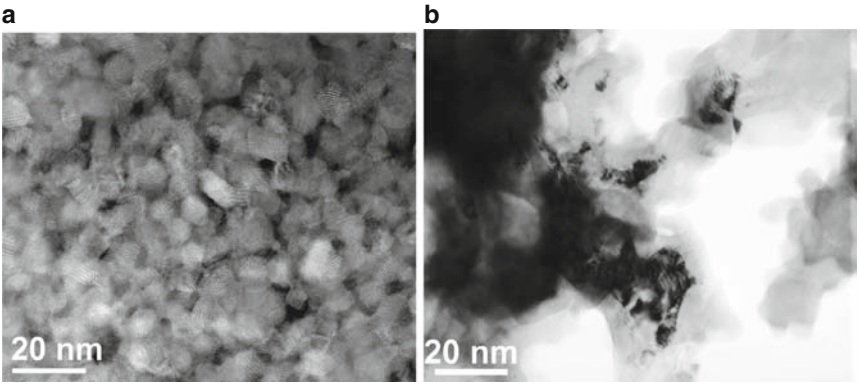

Fig. 8.8 (**a**) Bright field high-resolution electron micrograph of the nanograined Ce–Gd–Ni complex oxide thin film and (**b**) of the nanograined Y_2O_3 thin film deposited by the liquid ceramics technology

5 to 100 nm. The components in multicomponent films are distributed uniformly. This technology is extremely flexible. It permits to synthesize the oxides with various compositions and also to change the composition of oxides in the very broad interval. The possibility of tailoring the oxide doping allows one to develop the new advanced materials for the fuel cells and to reach the previously unattainable parameters of the fuel cells. Liquid ceramics method permits to change the grain size and influence the shape of grains (for example, from equiaxial, Fig. 8.8a, to pancake-like, Fig. 8.8b).

8.8 Conclusions

Nanostructured conducting oxides are very promising for various electronic and energy consumption applications like varistors, electrolytes for the SOFC, semipermeable membranes, and sensors. GB phases crucially determine the properties of nanograined oxides produced by powder sintering. GB phase transformations (wetting, prewetting, pseudopartial wetting etc.) proceed in the conducting oxides during sintering and following thermal treatments. Novel GB lines appearing in the conventional bulk phase diagrams permit the GB engineering and tailoring the properties of nanograined conducting oxides. Particularly useful are the novel synthesis methods for conducting oxides, like that of liquid ceramics.

Acknowledgements The authors thank the Russian Foundation for Basic Research (contracts 09-08-90406 and 09-03-92481). They also greatly appreciate Dr. W. Sigle and Dr. F. Phillipp (Max-Planck-Institut für Metallforschung, Stuttgart, Germany) for their help in the electron microscopy investigations.

References

1. H. Wang, Y.-M. Chiang, J. Amer. Ceram. Soc. **81**, 89 (1998)
2. J. Luo, H. Wang, Y.-M. Chiang, J. Amer. Ceram. Soc. **82**, 916 (1999)
3. Y.-M. Chiang, L.A. Silverman, R.H. French, R.M. Cannon, J. Amer. Ceram. Soc. **77**, 1143 (1994)
4. H. Duncan, A. Lasia, Solid State Ionics **176**, 1429 (2005)
5. M.-B. Park, N.-H. Cho, Solid State Ionics **154–155**, 407 (2002)
6. J.Y. Park, G.M. Choi, Solid State Ionics **154–155**, 535 (2002)
7. L.-S. Chang, E. Rabkin, B.B. Straumal, B. Baretzky, W. Gust, Acta mater. **47**, 4041 (1999)
8. B. Straumal, E. Rabkin, W. Lojkowski, W. Gust, L.S. Shvindlerman, Acta mater. **45**, 1931 (1997)
9. S.V. Divinski, M. Lohmann, Chr. Herzig, B. Straumal, B. Baretzky, W. Gust, Phys. Rev. B. **71**, 1041041 (2005)
10. J. Schölhammer, B. Baretzky, W. Gust, E. Mittemeijer, B. Straumal, Interface Sci. **9**, 43 (2001)
11. M. Matsuoka, Jap. J. Appl. Phys. **10**, 736 (1971)
12. L.M. Levinson, H.R. Philipp, Amer. Ceram. Soc. Bull. **65**, 639 (1986)
13. T.K. Gupta, J. Amer. Ceram. Soc. **73**, 1817 (1990)
14. F. Greuter, G. Blatter, Semicond. Sci. Technol. **5**, 111 (1990)
15. B. Bhushan, S.C. Kashyap, K.L. Chopra, J. Appl. Phys. **52**, 2932 (1981)
16. J. Wong, J. Appl. Phys. **51**, 4453 (1980)
17. J. Luo, Y.-M. Chiang, R.M. Cannon, Langmuir **21**, 7358 (2005)
18. J. Wong, J. Amer. Ceram. Soc. **57**, 357 (1974)
19. J. Wong, W.G. Morris, Amer. Ceram. Soc. Bull. **53**, 816 (1974)
20. F. Greuter, Solid State Ionics **75**, 67 (1995)
21. J.P. Gambino, W.D. Kingery, G.E. Pike, H.R. Philipp, J. Amer. Ceram. Soc. **72**, 642 (1989)
22. W.D. Kingery, J.B. van der Sande, T. Mitamura, J. Amer. Ceram. Soc. **62**, 221 (1979)
23. E. Olsson, L.K.L. Falk, G.L. Dunlop, J. Mater. Sci. **20**, 4091 (1985)
24. E. Olsson, G.L. Dunlop, J. Appl. Phys. **66**, 3666 (1989)
25. J.-R. Lee, Y.-M. Chiang, G. Ceder, Acta mater. **45**, 1247 (1997)
26. M. Safronov, V.N. Batog, T.V. Stepanyuk, P.M. Fedorov, Russ. J. Inorg. Chem. **16**, 460 (1971)
27. J.P. Guha, S. Kunej, D. Suvorov, J. Mater. Sci. **39**, 911 (2004)
28. D.R. Clarke, J. Appl. Phys. **49**, 2407 (1978)
29. D.R. Clarke, J. Amer. Ceram. Soc. **70**, 15 (1987)
30. F. Brochard-Wyart, J.-M. di Meglio, D. Quéré, P.G. de Gennes, Langmuir **7**, 335 (1991)
31. H.L. Tuller, A.S. Nowick, J. Electrochem. Soc. **122**, 255–259 (1975)
32. M. Filal, C. Petot, M. Mokchah, C. Chateau, J.L. Charpentier, Solid State Ionics. **80**, 27–35 (1995)
33. G. Petot-Ervas, C. Petot, Solid State Ionics **117**, 27 (1999)
34. A. Rizea, D. Chirlesan, C. Petot, G. Petot-Ervas, Solid State Ionics **146**, 341 (2002)
35. S.P.S. Badwal, Solid State Ionics **76**, 67 (1995)
36. M. Aoki, Y. Chiang, I. Kosacki, L.J. Lee, H. Tuller, Y. Liu, J. Amer. Ceram. Soc. **79**, 1169 (1996)
37. P. Mondal, A. Klein, W. Jaegermann, H. Hahn, Solid State Ionics **118**, 331 (1999)
38. G. Xu, Y.W. Zhang, C.S. Liao, C.H. Yan, Solid State Ionics **166**, 391 (2004)
39. E.P. Butler, J. Drennan, J. Amer. Ceram. Soc. **65**, 474 (1982)
40. M. Godickemier, B. Michel, A. Orlinka, P. Bohac, K. Sasaki, L. Gauckler, H. Henrich, P. Schwander, G. Kostorz, H. Hofmann, O. Frei, J. Mater. Res. **9**, 1228 (1994)
41. A.J. Feighery, J.T.S. Irvine, Solid State Ionics **121**, 209 (1999)
42. A. Yuzaki, A. Kishimoto, Solid State Ionics **116**, 47 (1999)
43. X. Guo, C.Q. Tang, R.Z. Yuan, J. Eur. Ceram. Soc. **15**, 25 (1995)
44. T.S. Zhang, J. Ma, L.B. Kong, S.H. Chan, P. Hing, J.A. Kilner, Solid State Ionics **167**, 203 (2004)
45. A. Tschöpe, S. Kilassonia, R. Birringer, Solid State Ionics **173**, 57 (2004)

46. A.R. Yavari, P.J. Desré, T. Benameur, Phys. Rev. Lett. **68**, 2235 (1992)
47. Y. Xu, M. Umemoto, K. Tsuchiya, Mater. Trans. **9**, 2205 (2002)
48. S. Ohsaki, K. Hono, H. Hidaka, S. Takaki, Scripta Mater. **52**, 271 (2005)
49. G.M. Wang, S.J. Campbell, A. Calka, W.F. Caczmarek, NanoStruc. Mater. **6**, 389 (1995)
50. S.J. Campbell, G.M. Wang, A. Calka, W.F. Caczmarek, Mater. Sci. Eng. A. **226–228**, 75 (1997)
51. S.M.M. Ramos, L. Amarai, M. Behar, G. Marest, A. Vasques, F.C. Zawislak, Radiat. Eff. Def. Sol. **110**, 355 (1989)
52. B.B. Straumal, B. Baretzky, A.A. Mazilkin, F. Phillipp, O.A. Kogtenkova, M.N. Volkov, R.Z. Valiev, Acta Mater. **52**, 4469 (2004)
53. A.A. Mazilkin, B.B. Straumal, E. Rabkin, B. Baretzky, S. Enders, S.G. Protasova, O.A. Kogtenkova, R. Z. Valiev Acta mater. **54**, 3933 (2006)
54. A.A. Myatiev, N.I. Diachenko, A.L. Pomadchik, P.B. Straumal, Nano- and Microsystem Technol. **3**, 19 (2005). In Russian